Chapter 5

Theoretical Analysis and Implementation of Photovoltaic Fault Diagnosis

Yihua Hu and Wenping Cao

Additional information is available at the end of the chapter

http://dx.doi.org/10.5772/62057

Abstract

The utilization of solar energy by photovoltaics (PVs) is seen in increase across the world since the technologies are getting mature and the material costs are being driven down. However, their operating costs are still very high, owing to their vulnerability to harsh outdoor environments they are working. Currently, the reliability of PV systems is the bottle-neck issue and is becoming a heated research topic. This chapter presents the state-of-the-art technologies for photovoltaic fault diagnosis, based on an intensive literature review and theoretical analysis. The chapter evaluates the fault mechanisms of photovoltaics at the cell, module, string and array levels. Analytical models are developed to understand the PV's terminal characteristics for diagnostic purposes. Offline and online fault diagnosis technologies are reviewed and compared based on the use of electrical sensors and thermal cameras. The aim of this chapter is to illustrate the PV faulty characteristics, to develop offline and online fault diagnosis, and to use the fault diagnosis information to achieve optimal operation (maximum power point tracking) under various PV faulty conditions, by using multi-disciplinary analytical, empirical and experimental methods.

Keywords: Fault diagnosis, MPPT, photovoltaics, solar energy, reliability

1. Introduction

Solar energy is the primary source of renewable energy. The generation of solar power using photovoltaic (PV) systems is gaining popularity in developed and developing countries across the globe because PV technologies are getting mature and the material costs are continuing to reduce. In this field, the operating costs are still high primarily due to the vulnerability of the PV panels at harsh operating environments. It is now a technical challenge to operate the PV system with a minimal interruption and a maximum power output. This chapter reviews and

develops the state-of-the-art technologies for PV fault diagnosis and maximum power point tracking (MPPT) by the intelligent control of direct current (DC)–DC converters. This chapter evaluates the fault mechanisms of photovoltaics at the cell, module, string, and array levels and reviews some of the fault diagnosis techniques. Analytical models are developed to understand the PV's terminal characteristics for fault diagnostic purposes. Offline and online fault diagnosis technologies are studied by using inexpensive electrical sensors and thermal cameras. The analysis of faulty characteristics and fault diagnosis of PV is conducted by using multidisciplinary analytical, empirical, and experimental methods. It is hoped to provide guidelines for developing economic solar power plants especially for the developing countries where solar energy utilization is a very cost-sensitive market.

2. PV faults

Photovoltaic (PV)-based solar power generation has proven to be a cost-effective and environmentally sustainable technology and, thus, it is under the rapid development over the last few decades. Nonetheless, it is presently hampered by relatively high operational costs, low system efficiency, and low effective service time (EST) of PV panels. A cost reduction roadmap for PV systems is illustrated in Fig. 1. In principle, there are two effective ways for achieving this. One is to increase the operating efficiency (and thus the yield) and the other is to extend the EST of the PV components. This chapter addresses both the issues by the intelligent control of the DC–DC converters for MPPT and the development of PV fault diagnosis technologies.

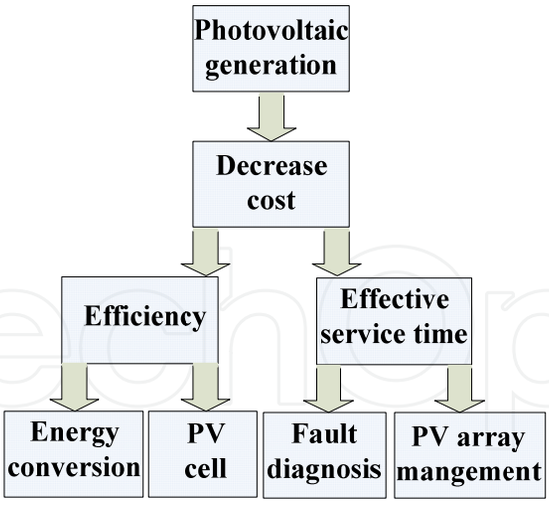

Figure 1. PV cost reduction roadmap.

PV system failures are typically caused by various types of faults or aging effect. In general, there are two types of faults in terms of their duration, temporary and permanent, as shown in Fig. 2. The temporary fault can be cleared automatically for a given time (e.g., shading) or by human intervention (e.g., dust), while the permanent fault is persistent or ongoing. Both the types can decrease the output of PV arrays. The temporary fault may be identified by

http://dx.doi.org/10.5772/62057

human eyes, but the permanent fault usually cannot be identified without special equipment (e.g., thermal camera) before a severe damage is made.

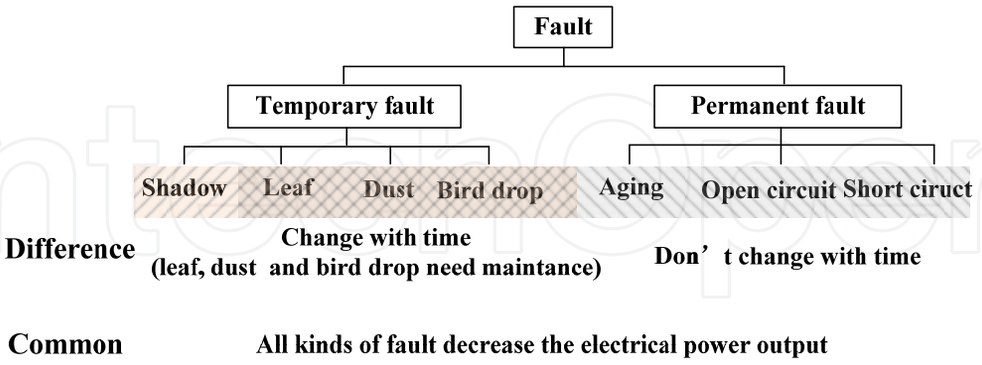

Figure 2. Types of PV faults.

Mismatch faults reduce the power output and cause potential damage to PV cells [1-10]. This section addresses both the issues by presenting a low-cost and efficient temperature-distribution analysis for identifying PV module mismatch faults using various technologies.

When a PV module is faulted or partial shading occurs, the PV system finds a non-uniform distribution of the generated electrical power and thermal profile, and the generation of multiple maximum power points (MPPs). If left untreated, this reduces the overall power generation and severe faults may propagate resulting in damage to the system [11-18]. In this chapter, any scenario that causes the output power of PV array to decrease is called a “fault.”

3. PV fault characteristics

This section defines fault categories and mathematical models in terms of PV components. A PV module is composed of dozens of PV cells in series connections. A large number of PV modules connected in series form a PV string, which can be connected in parallel to form a PV array, as shown in Fig. 3. In order to restrict the hotspot phenomena of a PV module, a bypass diode is connected in parallel with PV cells, and the corresponding structure is named a cell-unit, which is composed of m PV cells. The PV module is connected in series by n cell-units to achieve the high-output voltage. The PV string is composed of s PV modules that are also connected in series.

3.1. Category of PV faults

When a fault occurs in the PV array, a temperature difference between the healthy and an unhealthy module is created, similar to partial shading observed from the terminal. Consequently, excessive heat and thermal stress can result in cell cracks. If the cell temperature exceeds its critical point, delamination of cell encapsulants may occur. If the reverse bias exceeds the cell’s breakdown voltage, the cell will be damaged [19]. In terms of the severity of

mismatch faults, this chapter defines three categories: minor, medium, and heavy faults. Their terminal characteristics are different in the following aspects:

i. Under a minor fault, the faulted power unit in the PV panel can still operate to generate electricity. As illustrated by the single arrow in Fig. 4(a), the current still passes through the PV cell string to generate an output. In this case, the faulty cell becomes an electrical load, powered by the healthy ones.

ii. Under a medium fault, PV cells in the string are characterized by the varying illumination levels. As presented in Fig. 4(b), the faulted cells can still operate as a source with a reduced power output. Because of the nonuniform illumination, the actual working point of the power unit is dictated by the operating point of the PV array.

iii. Under a heavy fault condition, the whole PV string is out of function while the bypass diode conducts to transmit the current, as indicated by the dotted arrow in Fig. 4(a). In essence, all PV cells in the string are open-circuited.

If there exists a meaningful temperature difference, hotspot suppression is needed to shift the system MPP and to minimize the impact of the mismatch fault [15].

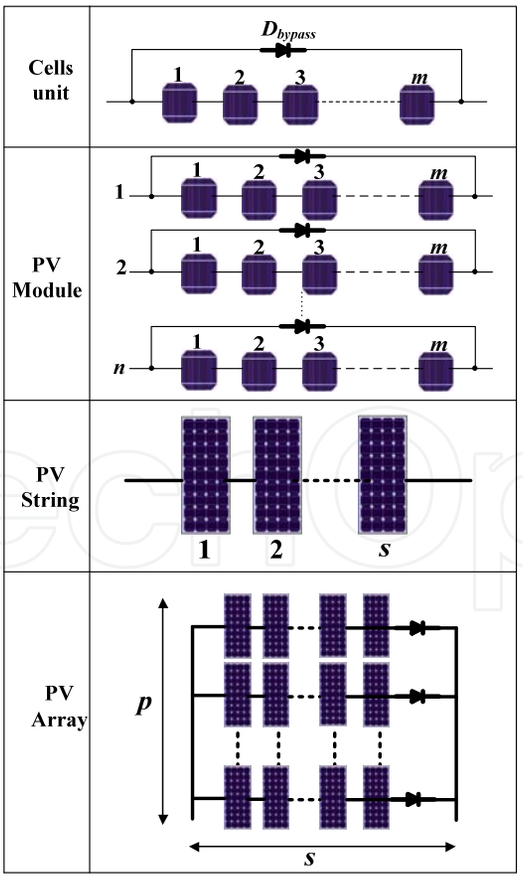

Figure 3. Component of PV arrays.

http://dx.doi.org/10.5772/62057

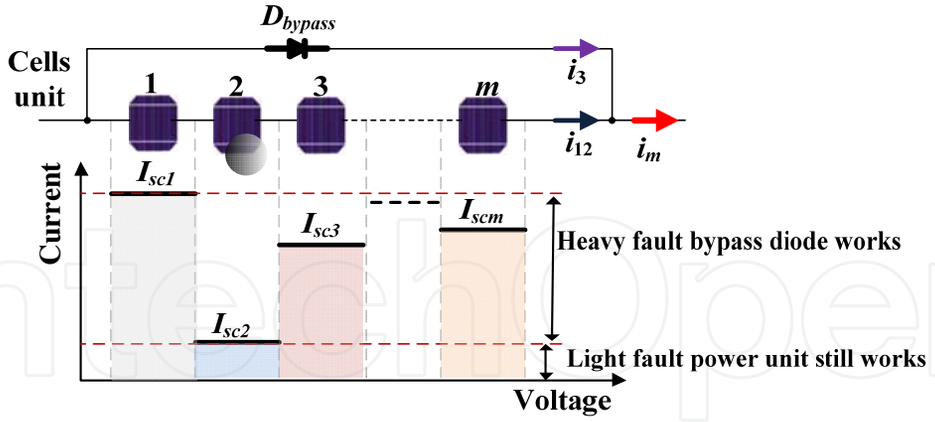

(a) Minor- and heavy-fault conditions

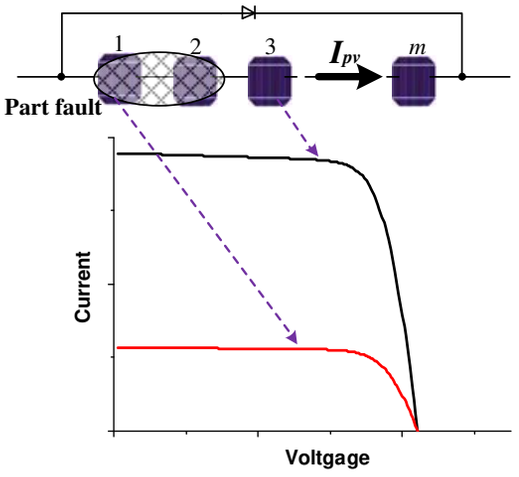

(b) Medium-fault condition

Figure 4. Three categories of mismatch faults defined for a PV system.

3.1.1. Analysis of minor faults

A temperature profile of the PV array under minor-fault conditions is presented in Fig. 5(a). The array consists of b rows and a columns of PV modules where Module 21 is faulted. I_{array} and V_{array} are the current and voltage of the PV array, respectively. I_{H} and I_{f} are the currents of healthy and faulty strings, respectively. V_{H} and V_{f} are the module voltages of healthy and faulty strings, respectively. T_{H} is the module temperature of a healthy string, $T_{\text{H}'}$ is the healthy module temperature within a faulted string, and T_{f} is the healthy cell temperature in a faulty power unit.

Under a PV minor fault, the faulty cell cannot generate electricity and becomes a resistive load (R_{eq}). Owing to the series of connection structure, the healthy cells supply power to the faulty

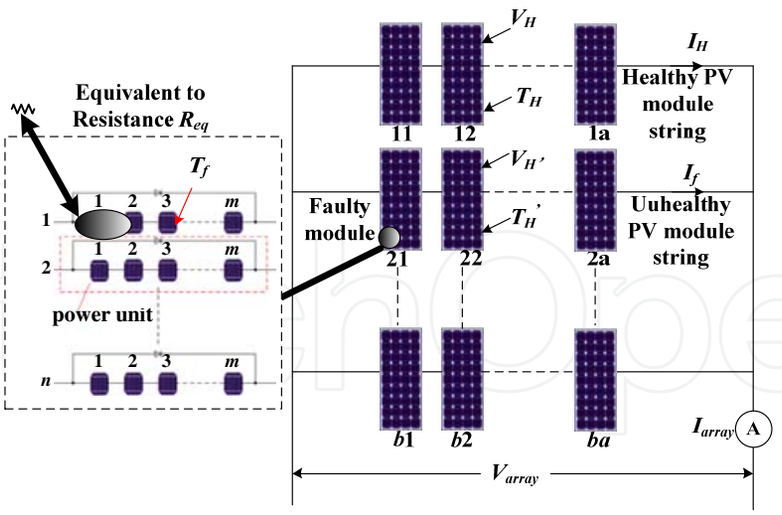

(a) Faulty PV array temperature distribution

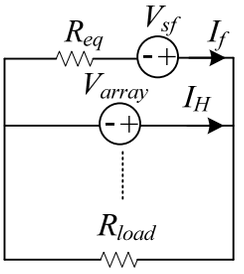

(b) Equivalent circuit upon a fault

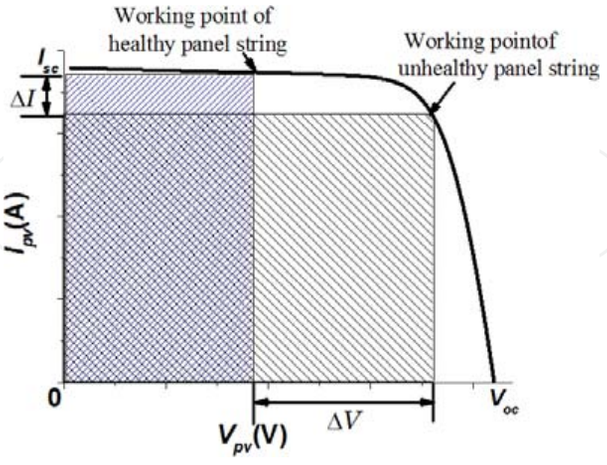

(c) Shift of working points

Figure 5. The PV system at a minor-fault condition [7].

http://dx.doi.org/10.5772/62057

PV cells (released as heat) and then create some hot spots. An equivalent circuit of the PV array is presented in Fig. 5(b), where V_{sf} stands for the voltage generated by the healthy PV cells in a faulty PV string and R_{load} is the load resistance.

The electric characteristics of a faulty PV string are:

$$V_{sf} - I_f R_{eq} = V_{array} \tag{1}$$

$$I_f = \frac{V_{sf}}{R_{eq} + R_{load}} \tag{2}$$

$$R_{eq} = \frac{V_{sf} - V_{array}}{I_f} \tag{3}$$

$$\Delta V = V_{H'} - V_H \tag{4}$$

$$\Delta I = I_H - I_f \tag{5}$$

$$I_f^2 \cdot R_{eq} < I_f (m - m_x) \frac{V_{H'}}{m \cdot n} \tag{6}$$

where ΔI is the current difference between the healthy and unhealthy strings, ΔV is the voltage difference between the healthy modules in healthy and unhealthy strings, and m_x is the number of faulty PV cells.

From Fig. 5(b), it can be seen the voltage of a PV cell in a healthy string is lower than that of a healthy cell in a faulty string; the current of a PV cell in a healthy string is higher than that of a healthy cell in a faulty string. Eqs. (4)–(6) express the mathematical relationship for faulty and healthy PV strings. Eq. (6) shows that when the output power of a faulted PV unit is higher than the I^2R power of its equivalent resistance, a minor fault is created and hot spots begin to form on the faulty cell.

Since the electrical power generated by healthy cells in the PV string supplies not only the load but also faulted cells (heating), the operating point in the current–voltage curve is effectively shifted. Fig. 5(c) demonstrates this in a PV system including healthy and unhealthy panel strings.

3.1.2. Analysis of heavy faults

Under a heavy-fault condition, the PV string containing the faulted cell/module loses production. Its operating points are illustrated in the output current–voltage curve in Fig. 6. Point A1 is the working point of the modules in the healthy string, A2 is the working point of the healthy

modules in the faulty string, and A3 is the working point of the healthy cells in the faulty module.

Because the faulty power unit is short-circuited by a bypass diode, the healthy cells in the faulty string are effectively open-circuited. The relative positions of A1, A2, and A3 are determined by the PV array structure and its electrical characteristics. Due to the anti-parallel connection of the bypass diode, the faulty PV power unit is shorted by the diode. Therefore, its output voltage becomes zero. From Eq. (8), V_H is less than V_H'; I_H is greater than I_f, corresponding to the working points A1 and A2. T_H and $T_{H'}$ depend on the working points A1 and A2 in the curve. As the faulty power unit is shorted by a bypass diode, the PV cells are open-circuited, corresponding to point A3. The output power of the faulted power unit is lower than the needed power of the equivalent resistance upon a fault; the power unit is shorted by the bypass diode.

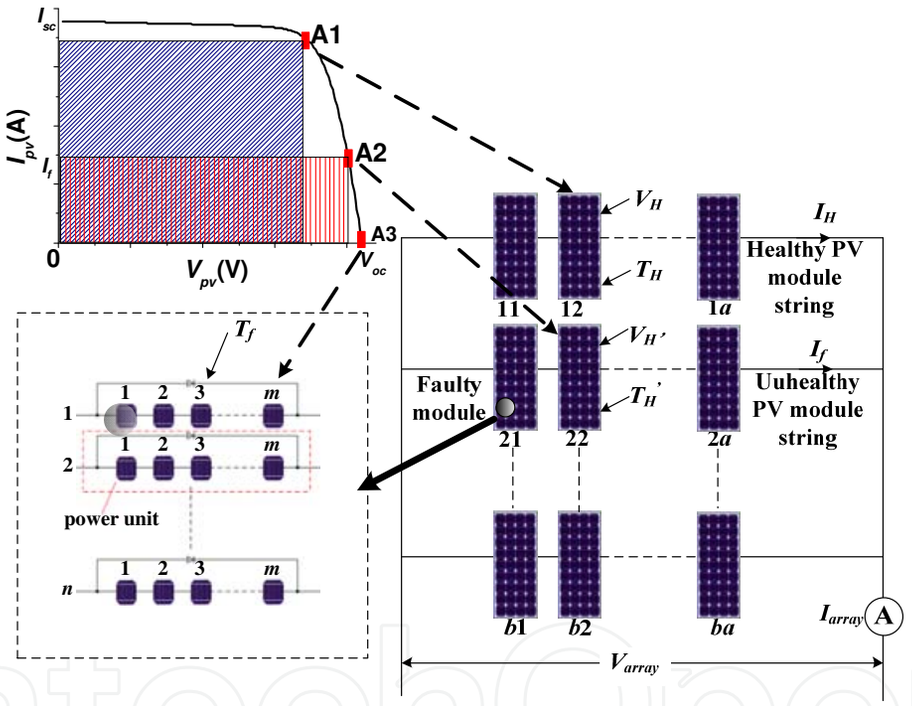

Figure 6. The PV system at a heavy-fault condition [7].

V_H and $V_{H'}$ are thus given by

$$V_H = \frac{V_{array}}{a} \tag{7}$$

$$V_{H'} = \frac{V_H \cdot a \cdot n}{a \cdot n - n_x} \tag{8}$$

http://dx.doi.org/10.5772/62057

where n_x is the number of faulty power units in the faulty PV panel string, which can be identified by thermal cameras.

3.1.3. Analysis of medium faults

The operating point of the PV array strongly affects the condition of the healthy PV modules in the healthy string and sometimes in the faulty string. Fig. 7(a) shows a 2×3 PV array under a medium fault, where module 21 is a faulted PV module, and the rest of the PV modules are healthy. Compared with other PV module (1000 W/m^2), No. 21 has the lower illumination (300 W/m^2). Fig. 7(b) and (c) presents the current–voltage and power–voltage curves, respectively, obtained from simulation.

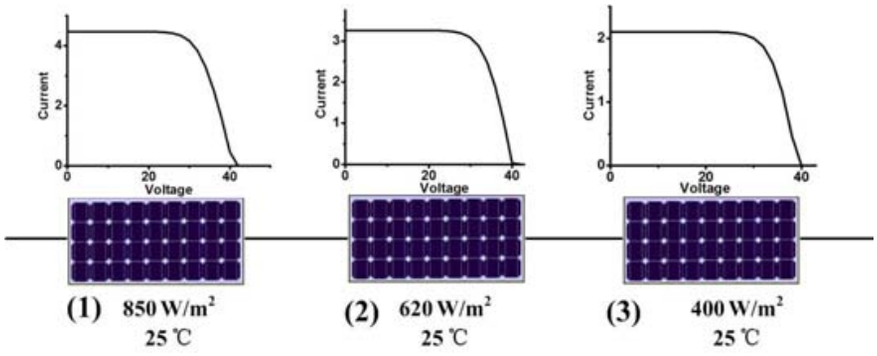

(a) PV string under medium-fault conditions

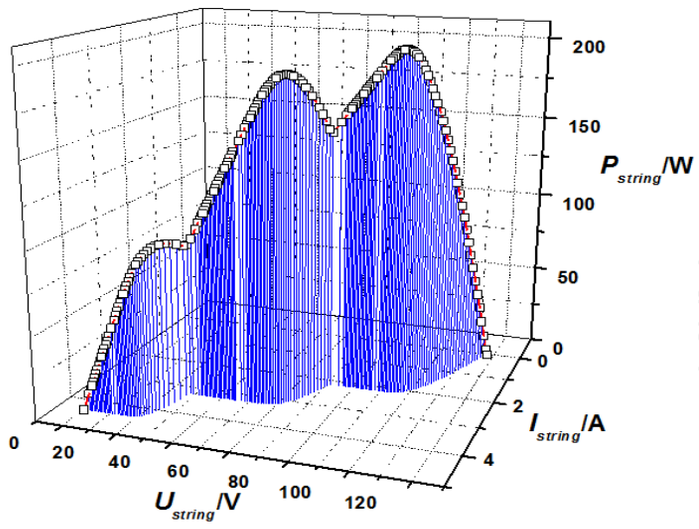

(b) Output characteristics of the medium faults

Figure 7. The PV system at a medium-fault condition.

Fig. 7 presents the typical output characteristics of the PV string under faulty conditions; the PV module simulation parameters are listed in Table 1. The string includes three modules with

nonuniform illumination, with the corresponding environment parameters being 850 W/m^2, 25°C; 620 W/m^2, 25°C; and 400 W/m^2, 25°C, as shown in Fig. 7(a). Each module has uniform illumination. In this current–voltage–power waveform, there are three local maximum power points, corresponding to three working stages, as tabulated in Table 2. At stage 1, the PV string current is between 3.29 and 4.39 A; only PV module No. 1 can generate that level of current and PV modules 2 and 3 are shorted. As they are influenced by shadows and cannot generate electricity, the string output voltage is limited to 0–30 V. At stage 2, the operation string current is between 2.19 and 3.29 A; PV modules 1 and 2 can generate electricity; No. 3 is shorted by the bypass diode. The corresponding PV string output voltage is 30–70 V. At stage 3, the operation string current is 0–2.19 A; all the modules can generate electricity and the string output voltage area is 76–126 V. From this analysis, it can be found that:

i. The multi-stage characteristics are caused by the differing output current ability of each module;

ii. In the high-output current area, the faulty modules are short-circuited, and the terminal voltage of the corresponding faulty module is zero.

Parameter	Value
Open-circuit voltage	44.8 V
Short-circuit current	5.29 A
Power output	180 W
MPP current	5 A
MPP voltage	36 V
Current-temperature coefficient	0.037 %/K
Voltage-temperature coefficient	–0.34 %/K
Power-temperature coefficient	–0.48 %/K
Nominal operating cell temperature	46 ± 2°C

Table 1. Specifications of the PV module

Working stage	Voltage	Current	Working module
1	0–30 V	3.29–4.39 A	1
2	30–72 V	2.19–3.29 A	1 and 2
3	76–126 V	0–2.19 A	1, 2, and 3

Table 2. Analysis of different stages

http://dx.doi.org/10.5772/62057

4. Mathematical models of PV systems

Under different fault conditions, the mathematical models vary as follows.

4.1. Model of healthy PV cells

The electrical characteristics of PVs are influenced by both temperature and illumination. The electrical model of the PV cell is expressed by [3]:

$$I = I_{\mathrm{L}} - I_{\mathrm{o}}[\exp(\frac{\varepsilon \cdot V}{T_{\mathrm{m}}}) - 1] \tag{9}$$

$$\varepsilon = \frac{q}{N_{\mathrm{s}} \cdot K \cdot A} \tag{10}$$

$$I_{\mathrm{L}} = \frac{G}{G_{\mathrm{ref}}}[I_{\mathrm{Lref}} + k_i(T_{\mathrm{m}} - T_{\mathrm{ref}})] \tag{11}$$

$$I_{\mathrm{o}} = I_{\mathrm{oref}}(\frac{T_{\mathrm{m}}}{T_{\mathrm{ref}}})^3 \exp[\frac{q \cdot E_{\mathrm{BG}}}{N_{\mathrm{s}} \cdot A \cdot K}(\frac{1}{T_{\mathrm{ref}}} - \frac{1}{T_m})] \tag{12}$$

where I is the PV module output current, I_{L} is the photon current, q is the quantity of electric charge, A is the diode characteristic factor, K is the Boltzmann constant, I_{o} is the saturated current, T_{m} is the PV module temperature, G is the irradiance, V is the output voltage, G_{ref} is the reference irradiance level (1000 W/m²), I_{Lref}, I_{oref} are the reference values for I_{L} and I_{o}. k_i is the current–temperature coefficient provided by the PV manufacturer, T_{ref} is the reference temperature, N_{s} is the number of series-connected cells, T_{m} is the PV module temperature, and ε is a constant depending on q, Ns, K, A, and is calculated using the following equation:

$$I_{\mathrm{sc\_ref}} - I_{\mathrm{mpp\_ref}} = \frac{I_{\mathrm{sc\_ref}}}{\exp(\frac{\varepsilon \cdot V_{\mathrm{oc\_ref}}}{T_{\mathrm{ref}}}) - 1}[\exp(\frac{\varepsilon \cdot V_{\mathrm{mpp\_ref}}}{T_{\mathrm{ref}}}) - 1] \tag{13}$$

where $I_{\mathrm{mpp\_ref}}$, $I_{\mathrm{sc\_ref}}$, $V_{\mathrm{mpp\_ref,}}$ and $V_{\mathrm{oc\_ref}}$ are the maximum power point (MPP) current, short-circuit current, MPP voltage, and open-circuit voltage at a reference condition, respectively, defined by the relevant standard.

4.1.1. Terminal characteristics of faulted cells

When a PV cell is subject to aging, a direct indication is its lower output power than normal. Due to the *p–n* junction characteristics of the PV cell, its open-circuit voltage only changes

slightly while the short-circuit current changes dramatically. In this chapter, we use the short-circuit current to sense the aging condition of PV cells.

Fig. 8 presents a cell-unit with m nonuniformly aged PV cells, where I_{sc1}, I_{sc2}, I_{sc3}... I_{scm} are the short-circuit current for cells *1*, *2*, *3*... *m*, respectively. There are three ranges in the current-voltage output characteristics. In Range 1, the maximum current is the minimum of all cells' current (I_{sc1}, I_{sc2}, I_{sc3}... I_{scm}) and all the cells generate electricity. Minor fault is a transitional interval. Its equivalent circuit is presented in Fig. 8, and its terminal output voltage is presented in Eq. (14). Due to a voltage drop on R_e, the output voltage of the cell-unit is lower than a healthy cell-unit.

$$\sum_{1}^{m-1} V_{\text{cell}\_i} - i_{12} \cdot R_{\text{e}} = V_{\text{cu}} \tag{14}$$

where V_{cell} is the output voltage of the PV cell, R_{e} is the equivalent resistance of aged PV cell, and V_{cu} is the output voltage of the cell-unit.

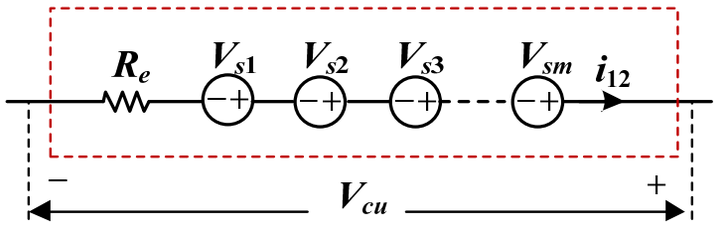

Figure 8. Equivalent circuit for the cell-unit at a minor fault.

As i_{12} increases, V_{cu} decreases to zero. The current switches from minor fault to heavy fault. In heavy fault, the cell-unit is bypassed by a diode, the corresponding terminal voltage is −0.5 V (i.e., diode voltage drop). In minor fault, the current passing the cell-unit i_j^q series-connected PV cells, the relationship between the output current i_{cu} and the terminal output voltage V_{cu}.depends on the operating points of the PV. To facilitate discussion on the three ranges, it is assumed that the magnitude of the short-circuit currents for m cells is

$$I_{sci_1} \le I_{sci_2} \le \cdots \le I_{sci_m} \tag{15}$$

where i_{cell} is defined as the actual current passing the PV cells. When the current i_{cell} starts to increase from 0 to $Isci_1$, all the cells generate electricity. When exceeds $Isci_1$ but less than Ici_2, cell i_1 cannot generate electricity; it is either bypassed or turned into a resistor because of the bucket effect. As a result, the relationship of i_{cu} and V_{cu} is summarized as follows.

If $i_{cell} \le Isci_1$, the unit-cell operates in normal condition:

http://dx.doi.org/10.5772/62057

$$i_{cu} = i_{cell} \le I_{sci_1} \tag{16}$$

$$V_{cu} = mV_{cell} \tag{17}$$

where V_{cell} is equal to the voltage of every cell.

If i_{cell}>$Isci_1$, the cell-unit operates in heavy fault:

$$V_{cu} = -0.5\text{V} \tag{18}$$

$$i_{cell} = 0 \tag{19}$$

$$i_{cu} = i_{diode} \tag{20}$$

Where i_{diode} is the bypass current flowing through the diode.

The PV cells can work in minor fault if there exists an integer $k<m$. to satisfy the following conditions:

$$I_{\text{sc}i_k} < i_{cell} \le I_{\text{sc}i_{k+1}}$$

$$(m-k)V_{cell} - i_{cell}\sum_{j=1}^{k} R_{ej} \ge 0 \tag{21}$$

When the cell-unit operates with a minor fault,

$$i_{cu} = i_{cell} \text{ and } V_{cu} = (m-k)V_{cell} - i_{cell}\sum_{j=1}^{k} R_{ej} \tag{22}$$

where R_{ej}.is the equivalent resistance of the jth cell.

Usually, normal operation and heavy fault are the steady-state operational conditions while minor fault is a short transitional range between the two and can often be ignored.

4.1.2. PV strings with nonuniformly faulty PV modules

A PV string consists of s V modules, with the terminal voltage V_{string}.and current i_{string}. Let the terminal voltage, current, and maximum current from the k PV module be $V_{module,k}$, $i_{module,k}$, and $i_{module,\,k}^{max}$ respectively. The following relationship can be established:

$$i_{string} = i_{module,1} = i_{module,2} = \cdots = i_{module,s} \tag{23}$$

$$V_{string} = V_{module,1} + V_{module,2} + \cdots + V_{module,s} \tag{24}$$

Similarly, the bucket effect indicates that the maximum current in the PV string is limited by the minimum $i_{module,\,k}^{max}$ f those non-bypassed modules. That is $i_{string} \le i_{module,\,k}^{max}, \quad 1 \le k \le s,$ and the kth module is not bypassed.

In practice, the cell-units within a PV module may be aged differently and thus have different maximum short-circuit currents. This case is called the "general non-uniform aging" in this chapter. A simpler case for nonuniformly aged PV modules is that all cell-units in the same PV module are aged uniformly so that the whole PV module can be characterized with a single maximum short-circuit current of any cell-unit. This is termed the simplified nonuniform aging in this chapter.

4.1.3. PV array with nonuniformly aged PV strings

A PV array consists of p parallel-connected PV strings; its terminal voltage and current are denoted by V_{array} and i_{array}, respectively. Let the terminal voltage and current for the jth PV string be $V_{array,j}$ and $i_{array,j}$,.respectively. Therefore,

$$i_{array} = i_{array,1} + i_{array,2} + \cdots + i_{array,p} \tag{25}$$

$$V_{array} = V_{array,1} = V_{array,2} = \cdots = V_{array,p} \tag{26}$$

The power output from the PV array is the sum of p strings and is also limited by the bucket effect. That is, the maximum power output from the simplified nonuniform aging PV array can be written as $\sum_{j=1}^{p} \min\left\{P_{j,k}^{max} : 1 \le k \le s, \quad \text{and the } (j,\,k) \text{ th module is un-bypassed } \right\}$ where $P_{j,k}^{max}$ is the maximum power output from the un-bypassed PV module at the position (j, k)(kth module in the jth string) of the PV array. $i_{module,\,j,k}$.is defined as the maximum short-circuit current in the (j,k). module; b and q as the number of PV modules in the jth string which generate electricity. Thus, (s-q). PV modules are bypassed by diodes in the jth string. Then, the maximum power $P_{j,k}^{max}$ is calculated as

$$P_{j,k}^{max} = qV_{module} i_j^q \tag{27}$$

http://dx.doi.org/10.5772/62057

where V_{module}.is the MPP voltage supplied by a PV module, and i_j^q is the qth largest short-circuit current within the set { $i_{module,j,1}$, $i_{module,j,2}$, …, $i_{module,j,s}$ }. For a normal PV module consisting of three cell-units, V_{module}=3$V_{cu.}$, and V_{cu} is the MPP voltage a PV cell-unit can provide.

5. PV array fault diagnosis and optimized operation

In this section, PV array fault diagnosis methods are reviewed and developed. Especially, PV fault diagnosis based on electrical sensors is proposed for small-scale PV array systems; thermal cameras are proposed for large-scale PV arrays; and optimized operation strategies under faulty conditions are also developed.

5.1. Existing fault diagnosis methods

Currently, thermal cameras, earth capacitance measurements (ECM), and time domain reflectometry (TDR) are three popular methods for PV fault diagnosis. In this section, the basic principles of those fault diagnosis are introduced [16, 20-34]. In the beginning of installation, ECM is an effective method to check the disconnection position of transmission line [23]. Due to the characteristics of PV modules, there is capacitance to ground existing in each module [35]. The capacitance to ground can be used to realize disconnection point location that is the theory of ECM. When the PV string has the disconnection point x_f, the disconnection module (x_f) from the positive node point to the fault point is calculated using the ratio of the earth capacitance values to the fault point and that of the whole line as shown in Fig. 9 and Eq. (28). Here, M is the total number of modules in the faulty string.

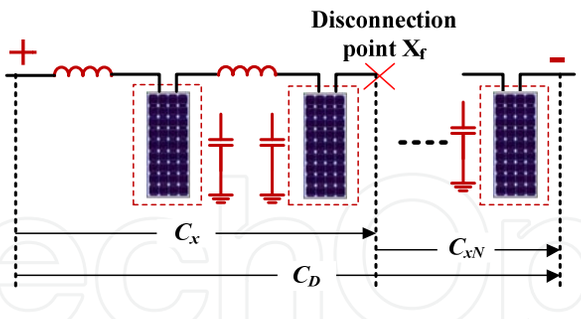

Figure 9. Fault diagnosis theory of ECM.

$$x_f = (C_x / C_D)M \tag{28}$$

For TDR, by injecting the signal into the transmission line, the signal will be distorted when mismatch is occurred [24]. Like a radar, the TDR method analyses the input signal and output signal, as shown in Fig. 10; the faulty point can be located and even aging condition can be estimated. But the illumination can influence the impedance of PV cell; therefore, TDR can only be used in the night.

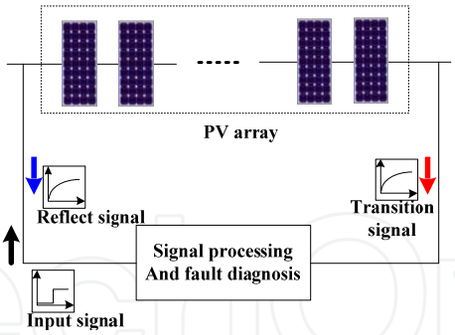

Figure 10. Theory of TDR.

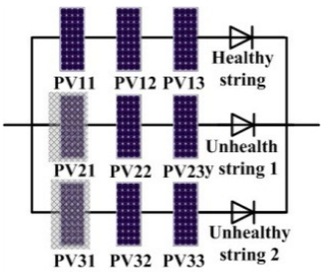

(a) Faulty 3×3 PV array

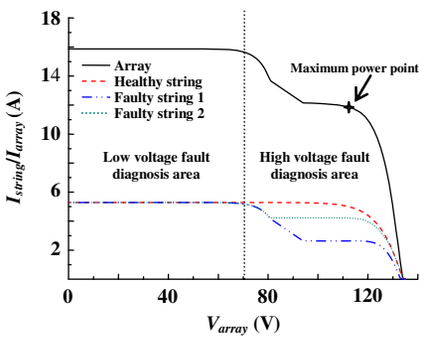

(b) Output characteristics

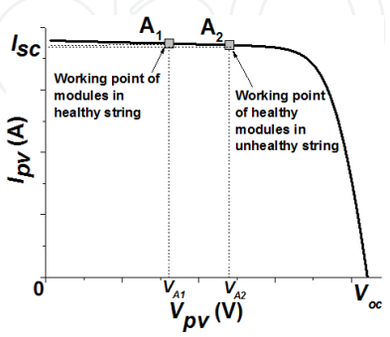

(c) Working points in the voltage fault diagnosis area

Figure 11. PV array under fault conditions.

http://dx.doi.org/10.5772/62057

The ECM can locate the disconnection of PV modules in the string while the TDR technology can predict the degradation of the PV array. Nonetheless, both ECM and TDR can only operate offline [23-24].

In practice, the online methods are highly demanded, which can take measurements while the tested device is in operation. To improve this, an automatic supervision and fault detection are proposed [25-26], based on power loss analysis. However, it requires surrounding environmental information and cannot identify the faulty module. An operating voltage window is then developed based on the PV string operation voltage and ambient temperature [27]. It can locate the open and short faults but still cannot identify the faulty module from the array. Currently, both offline and online fault diagnosis methods have been developed. Offline fault diagnosis cannot give real-time fault information that is the key factor for PV array optimization operation under fault condition. Currently, online fault diagnosis methods suffer from high costs or incapability of locating fault modules. A model-based reconfiguration algorithm is developed by [28] to realize the fault tolerance operation. But it needs a large number of electrical relays to reconfigure PV arrays. A similar technology, the *in situ* rearrangement strategy, can decrease the influence of shadow [29-32]. However, its success depends on three conditions: (i) a large number of relays need to be used; (ii) the health state of each PV module should be monitored; (iii) high-computing resource of the controller is required to calculate complex optimal arrangements. These increase the system cost and control complexity. An improved strategy is developed in [33], which not only needs the combination of power channels and relay matrix to combat the shadow influence but it also needs the healthy state of PV modules. A fingerprint curve of the PV array under shading conditions is proposed in [34] to find the key information (e.g., open-circuit and short-circuit points and MPP region) but it cannot locate the faulted modules.

5.2. PV fault diagnosis by using electrical sensors

It is clear that online fault diagnosis is important because: (i) it is the prerequisite for any array dynamical reconfiguration; (ii) it can provide crucial information for global MPPT; and (iii) it contains key state-of-health information useful for system maintenance. In this section, low-cost fault diagnosis for low-scale PV array and fault diagnosis strategy for large PV array fault diagnosis are proposed, respectively.

5.2.1. Fault diagnosis theory

When a PV array is faulted, the faulty module has lower illumination than healthy modules (e.g., a 3×3 array). Fig. 11(a) shows a multi-string faulty condition and Fig. 11(b) shows its output voltage–current characteristics. The output waveforms can be divided into two sections: the high-voltage fault diagnosis area and low-voltage fault diagnosis area (constant output current). In the latter area, the faulty module in the faulty string is shorted by bypass diodes where both healthy string and unhealthy string have the same current. PV string current sensors cannot distinguish the unhealthy string from healthy strings. Nevertheless, the healthy modules in the faulty string have a higher output voltage than the modules in the healthy

string, illustrated as points A1 and A2 in Fig. 11(c). The voltage difference between the healthy module in the unhealthy string and module in the healthy string can be employed to locate the faulty module.

For a p row s column array, assume that there is x faulted modules in the unhealthy string. V_{A1} and V_{A2} can be expressed as Eqs. (29) and (30):

$$V_{A1} = \frac{V_{array}}{s} \tag{29}$$

$$V_{A2} = \frac{V_{array}}{s - x} \tag{30}$$

In Fig. 11(a), V_{A1} is the corresponding healthy string module voltage, such as No. PV11; V_{A2} is the normal module voltage in the unhealthy string, such as No. PV22.

5.2.2. Optimized sensor placement strategy

In order to achieve the PV array fault diagnosis, the reading of PV module voltage is needed. Due to the large number of PV modules employed, a large number of voltage sensors are also needed in the first instance.

There are three basic sensor placement methods, as shown in Fig. 12. In the PV array, in method 1, each module terminal voltage is measured by a voltage sensor; the total number of sensors is p×s. In method 2, each voltage sensor measures the voltage between two nodes in the same column of adjacent strings; and (p-1)×(s-1) voltage sensors are needed. In method 3, the electric potential difference of adjacent modules is measured; the corresponding number of sensors is p×(s-2). The large number of voltage sensors may increase system capital cost and information-processing burden. Therefore, the voltage placement method needs to be optimized.

Fig. 13 shows an equivalent PV matrix where a PV module is shown as a dot; the connection line of the adjacent module is represented by a node. The proposed voltage placement strategy is developed by the following steps:

i. All the nodes should be covered by voltage sensors.

ii. A sensor can only connect one node in a string.

iii. Voltage sensor nodes cover different isoelectric points from different strings.

iv. If p or s is an even number, each node is connected to and only to one sensor. If both p and s are odd, there is one and only one node to be connected to two different sensors, while each of the remaining nodes is connected to one sensor.

http://dx.doi.org/10.5772/62057

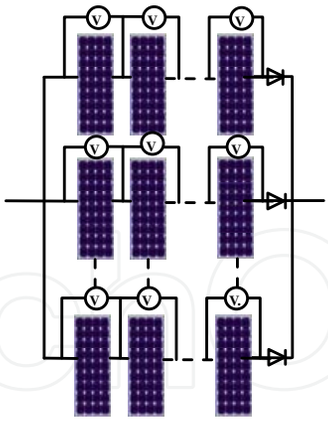

(a) Method 1

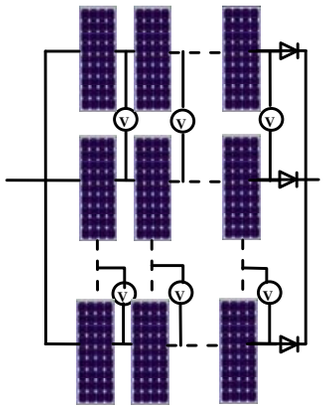

(b) Method 2

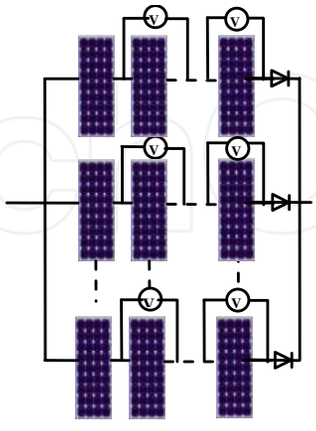

(c) Method 3

Figure 12. Sensor placement methods.

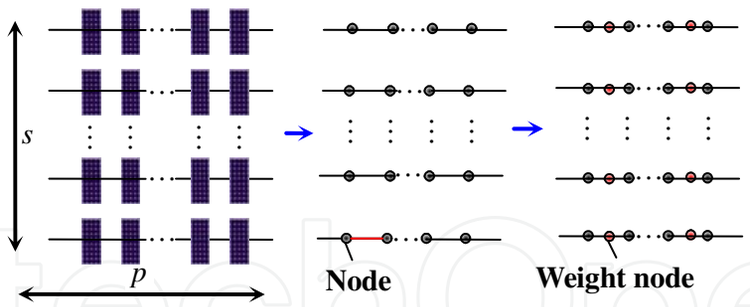

Figure 13. Equivalent matrix.

Fig. 14. presents an example of the 3×3 PV array. According to the proposed sensor placement strategy, only three voltage sensors are needed.

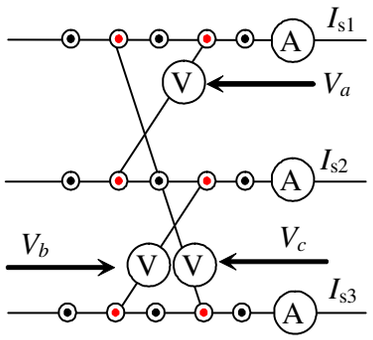

Figure 14. Simplified voltage sensor placement method for a 3×3 PV array.

A general principle is that the minimum number of sensors used to detect all possible faults should be [p×(s-1)/2] where the notation [a] is the ceiling function representing the smallest integer, which is not less than a. When a node is not connected to a sensor, the two adjacent PV modules of this node cannot be discriminated once a fault occurs at one of the two modules. The total number of nodes is equal to [p×(s-1)/2]. This is summarized in Table 3. It is clear that the proposed method can decrease the number of voltage sensors used compared with the other three methods.

Method	1	2	3	Proposed
No.	p× s	(p-1)×(s-1)	p×(s-2)	p×(s-1)/2

Table 3. Number of voltage sensors used by different methods

5.2.3. Mathematical model of proposed sensor placement strategy

The variable a_{ij} is defined as the healthy state of the PV module sitting at the i-th string and j-th module (denoted by (i, j)).in the p×s. array. If this module is healthy, then a_{ij}.=1, otherwise

http://dx.doi.org/10.5772/62057

$a_{ij.}$=0. The terminal voltage of the (*i, j*) module is denoted by u_{ij}, and the reading of a voltage sensor connecting the (*i, j*) module and another module sitting at the (*r, k*) position is denoted by $R_{i,j,r,k.}$. Without loss of generality, consider the case that each string has at least one healthy module. According to the voltage division law and the fact that the number of healthy modules in the *i*-th string equalizes $a_{i1} + a_{i2} + \ldots + a_{is}$, the terminal voltage u_{ij} of the (*i, j*) module is equal to a fraction of U_{array} and this fraction is 0 if a_{ij}=0., and is 1/ $(a_{i1} + a_{i2} + \ldots + a_{is})$ if a_{ij}=1 That is,

$$u_{ij} = \frac{a_{ij} U_{array}}{a_{i1} + a_{i2} + \cdots + a_{is}} \tag{31}$$

Note that the total output voltage of the modules (*i,* 1), (*i,* 2),..., and (*i, j*) is the sum of the terminal voltage of each of these *j* modules (i.e.,). Similarly the total output voltage of the modules (*r,* 1), (*r,* 2),..., and (*r, k*) equalizes. Therefore, the voltage reading of connecting the (*i, j*) module and the (*r, k*) module is calculated as:

$$\begin{aligned} R_{i,j,r,k} &= (u_{i1} + u_{i2} + \cdots + u_{ij}) - (u_{r1} + u_{r2} + \cdots + u_{rk}) \\ &= \frac{(a_{i1} + a_{i2} + \cdots + a_{ij}) U_{\text{array}}}{a_{i1} + a_{i2} + \cdots + a_{is}} - \frac{(a_{r1} + a_{r2} + \cdots + a_{rk}) U_{\text{array}}}{a_{r1} + a_{r2} + \cdots + a_{rs}} \end{aligned} \tag{32}$$

These provide a solution to the unknowns a_{ij} When the working point of a PV string moves to the high-voltage area, the voltage output of the healthy modules increases until reaching the open-circuit output voltage ; faulted modules in the string will equally divide the remaining voltage Therefore, the following relations hold for a string including both healthy and unhealthy modules:

$$\begin{aligned} u_{ij} &= a_{ij} U_{oc} + \frac{(1 - a_{ij})(U_{\text{array}} - (a_{i1} + a_{i2} + \cdots + a_{is}) U_{oc})}{s - (a_{i1} + a_{i2} + \cdots + a_{is})} \\ &= \frac{(a_{ij} s - (a_{i1} + a_{i2} + \cdots + a_{is})) U_{oc}}{s - (a_{i1} + a_{i2} + \cdots + a_{is})} + \frac{(1 - a_{ij}) U_{\text{array}}}{s - (a_{i1} + a_{i2} + \cdots + a_{is})} \end{aligned} \tag{33}$$

$$\begin{aligned} R_{i,j,r,k} &= (u_{i1} + u_{i2} + \cdots + u_{ij}) - (u_{r1} + u_{r2} + \cdots + u_{rk}) \\ &= \frac{(s \sum_{l=1}^{j} a_{il} - j \sum_{l=1}^{s} a_{il}) U_{oc}}{s - \sum_{l=1}^{s} a_{il}} + \frac{(j - \sum_{l=1}^{j} a_{il}) U_{\text{array}}}{\sum_{l=1}^{s} a_{rl}} \\ &\quad - \frac{(s \sum_{l=1}^{k} a_{rl} - k \sum_{l=1}^{s} a_{rl}) U_{oc}}{s - \sum_{l=1}^{s} a_{rl}} - \frac{(k - \sum_{l=1}^{k} a_{kl}) U_{\text{array}}}{\sum_{l=1}^{s} a_{rl}} \end{aligned} \tag{34}$$

The reading at the high-voltage status provides extra equations to solve the fault status variable That is, the system of Eqs (33) and (34) can be applied to determine the fault status variable.

It is observed that the placement of voltage sensors has two features. First, it is noted that the fault diagnosis problem is always solvable by placing voltage sensors only. This is because that if each PV module is installed with a voltage sensor, a PV fault can be detected from the terminal. Second, if there are always some methods to find the optimal sensor placement for any 2×*s* and 3×*s* PV arrays with the least number of sensors $(s-1)$ and $3\times(s-1)/2$, respectively, these methods do not need the existence of any healthy strings. Then, there is a way to design the optimal sensor placement for any general *p*×*s* array with $p\times(s-1)/2$.sensors. The reason is explained as follows. When *p* is an even number, the *p*×*s* array can be divided into $\frac{p}{2}$ blocks of 2×*s* arrays. For each block of the 2×*s* array, it needs to apply the existing optimal sensor placement method to achieve the optimal $\frac{p}{2}\times s$ sensors. If *p* is odd, the *p*×*s*. array consists of one 3×*s* array and blocks of 2×*s*.arrays. It needs to apply the existing sensor placement method for these small blocks where the number of sensors is equal to $[3\times(s-1)/2]+\frac{p-3}{2}(s-1)$.. By considering both even and odd cases, it can be found that:

$$\left[3\times(s\text{-}1)/2\right]+\frac{p-3}{2}(s-1)=\left[p\times(s\text{-}1)/2\right] \tag{35}$$

Therefore, the optimal number of sensors can be obtained.

5.2.4. Locating the faulted PV module in uniform faulty PV modules

By the reading of current sensor in high-output voltage area, the unhealthy string can be located. After locating the unhealthy string, the next step is to find the faulty PV module. In the low-voltage fault diagnosis area, the faulty modules are shorted; the corresponding fault diagnosis eigenvalue of the mono-string faulty module is presented in Table 4, where the fully faulty module indicates that all cell-units in the module are faulty. No. 7 is the extreme case that all the modules in this string are faulty. Even though the PV array works in the low-voltage area, the modules are open-circuited when all modules are faulty. Table 5 shows the multi-string characteristic values, from which the faulty module can be identified easily.

PV31–PV33	V_a	V_b	V_c
100	$V_{array}/3$	$2V_{array}/3$	$V_{array}/6$
10	$V_{array}/3$	$V_{array}/6$	$V_{array}/6$
1	$V_{array}/3$	$V_{array}/6$	$2V_{array}/3$
110	$V_{array}/3$	$2V_{array}/3$	$-V_{array}/3$
11	$V_{array}/3$	$-V_{array}/3$	$2V_{array}/3$
101	$V_{array}/3$	$2V_{array}/3$	$2V_{array}/3$
111	$V_{array}/3$	$2V_{array}/3-V_{oc}$	$2V_{oc}-V_{array}/3$
0	$V_{array}/3$	$V_{array}/3$	$V_{array}/3$

Table 4. Characteristic values for the mono-string fully faulted modules (0: healthy, 1: faulty)

PV11–PV13/PV21–PV23	*V*a	*V*b	*V*c
100/100	$V_{array}/2$	$V_{array}/6$	$2V_{array}/3$
010/100	$V_{array}/2$	$V_{array}/6$	$V_{array}/6$
001/100	V_{array}	$V_{array}/6$	$V_{array}/6$
100/010	$V_{array}/6$	$V_{array}/6$	$2V_{array}/3$
010/010	$V_{array}/6$	$V_{array}/6$	$V_{array}/6$
001/010	$V_{array}/2$	$V_{array}/6$	$V_{array}/6$
100/001	0	$2V_{array}/3$	$2V_{array}/3$
010/001	0	$2V_{array}/3$	$V_{array}/6$

Table 5. Characteristic values for multi-string fully faulted PV modules

5.2.5. Locating faulty PV module in uniform faulty PV module

Both Tables 4 and 5 deal with the fully faulted module where all cell-units are faulted while a partially faulted module widely occurs where some cell-units are faulted. Usually, partial shadow is also accrued in one PV module. Due to the cell-unit structure of PV modules, even when only one cell is faulty (0 W/m^2), the whole cell-unit output power will decrease dramatically. Fig. 15(a) presents experimental results of the faulty cell-unit that is composed of 24 PV cells with only one faulty PV cell. The faulty cell-unit maximum output power is 4.75 W while that of healthy cell-unit is 48 W, making a loss of 90 %. From Fig. 15, we conclude that PV cell-unit cannot work when a cell fault occurs.

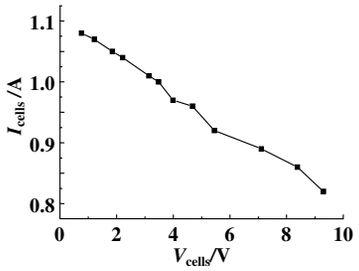

(a) PV cell-unit output under fault conditions

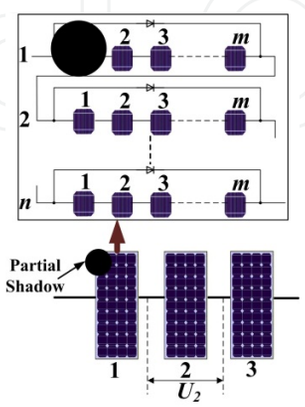

(b) Partial shadow

Figure 15. PV string under partial shadow conditions.

Therefore, when a PV module endures partial shadowing, its terminal output voltage is lower than the healthy module and higher than zero. In Fig. 15(b), PV module No. 1 loses one of the cell-unit, the PV module output voltage is reduced to $\frac{n-1}{n}$ of the healthy module output voltage.

Therefore, PV string fault diagnosis can be achieved by measuring the PV module voltage, which changes with the string working point. When the string works in the high-current output area, the faulty PV module can be located because its output voltage is zero (unified shading) or lower than the healthy module (partial shading). Table 6 gives the typical eigenvalue under nonuniform PV module faulty condition.

PV11–PV13	V_a	V_b	V_c	Comparison
100	$V_{array}/6<V_a<V_{array}/3$	$V_{array}/3$	$V_{array}/3<V_c<2V_{array}/3$	—
10	$V_{array}/6<V_a<V_{array}/3$	$V_{array}/3$	$V_{array}/6<V_c<V_{array}/3$	—
1	$V_{array}/3<V_a<2V_{array}/3$	$V_{array}/3$	$V_{array}/6<V_c<V_{array}/3$	—
110	$V_a<V_{array}/3$	$V_{array}/3$	$V_{array}/3<V_c<2V_{array}/3$	$2V_a<V_c<V_{array}$
11	$V_{array}/3<V_a<2V_{array}/3$	$V_{array}/3$	$V_c<V_{array}/3$	$V_a<2V_c<V_{array}$
101	$V_a<V_{array}/3$	$V_{array}/3$	$V_{array}/3<V_c<2V_{array}/3$	$V_a<2V_c"/>V_{array}$

Table 6. Characteristic values for the mono-string partially faulted modules

6. Experimental verification

A 3×3 PV array is built to verify the proposed fault diagnosis technique. The PV modules are the same as used for simulation, and the environment illumination is recorded by TS1333R.

6.1. Sensor-based PV fault diagnosis

In this experiment, typical fault scenarios are studied and the sensor readings are compared with eigenvalue in the high-voltage and low-voltage fault diagnosis areas to check the effectiveness of the proposed fault diagnosis technique.

Fig. 16 shows the mono-string, mono-module fault diagnosis. In the fault scenario 1 (see Fig. 16(a)), the illumination is 550 W/m^2 and temperature is 15℃. The P33 PV module is cast by shadow manually to emulate a fault. Fig. 16(b) shows the current–voltage output characteristics of faulty PV array. Due to the fault on module P33, string 3 cannot generate electricity in the output voltage range 82–120 V. Fig. 16(c) presents the sensor output curves. In the low-voltage area (10–70V), the sensor is V_a and the output voltage is $V_{array}/3$. This is a normal output voltage and the corresponding strings are healthy. That is, strings 1 and 2 connected by this sensor are healthy, which coincides with fault scenario 1 in Fig. 16(a). Fig. 16(e) illustrates the high-voltage and low-voltage fault diagnosis areas. In the low-voltage area, the reference

http://dx.doi.org/10.5772/62057

eigenvalue is $V_{array}/6$; and in the high-voltage diagnosis area, the reference eigenvalue is $2V_{array}/3$-V_{oc}. The fact that the sensor V_b output is close to the reference value also verifies the proposed diagnosis method. The reference eigenvalue of V_c is $2V_{array}/3$; and the corresponding V_c sensor output also agrees with the reference eigenvalues. There is a slight deviation between V_a, V_b, and V_c and their reference values. This is caused by the diode voltage drop and the minor product irregularity between PV modules. From the sensor output results and information in Table 5, the fault type is classified as "001." The faulty module is P33 that also agrees with fault scenario 1 (Fig. 16(a)).

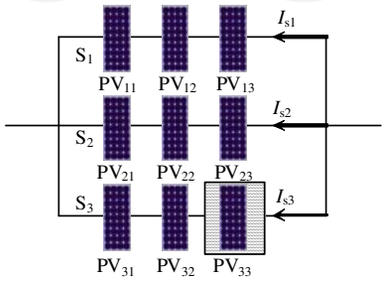

(a) Fault scenario

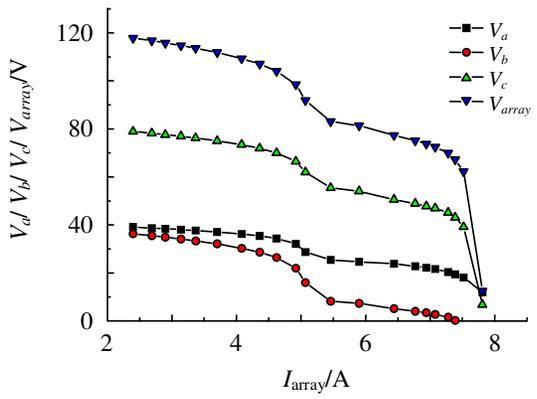

(b) Voltage sensor

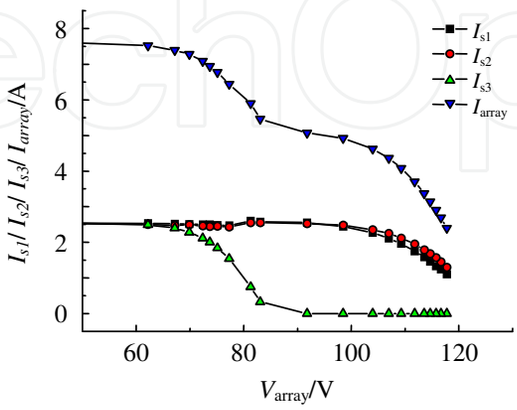

(c) Current sensor

Figure 16. Mono-string mono-module fault diagnosis.

Fig. 17 shows the multi-string mono-module fault diagnosis. In fault scenario 2, the illumination is 580 W/m^2 with the temperature of 25℃. The P11 module in string 1 and P33 module in string 3 are cast by shadow manually to simulate faulty conditions. Fig. 17(b) presents the current–voltage output characteristics of the faulty PV array. Due to a fault that occurred in modules P11 and P33, strings 1 and 3 cannot generate electricity over the output voltage range 82–120 V. In the low-voltage area, the sensors *a* and *b* have the same output (V_a=V_b=V_{array}/6), as illustrated in Fig. 17(c). The voltage sensors *a* and *b* also satisfy the rule for locating healthy strings. Therefore, string 2 is diagnosed as being healthy, which coincides with the fault scenario in Fig. 17(a). Fig. 17(d) shows fault diagnosis progress. The faulty modules identified are P11 and P33.

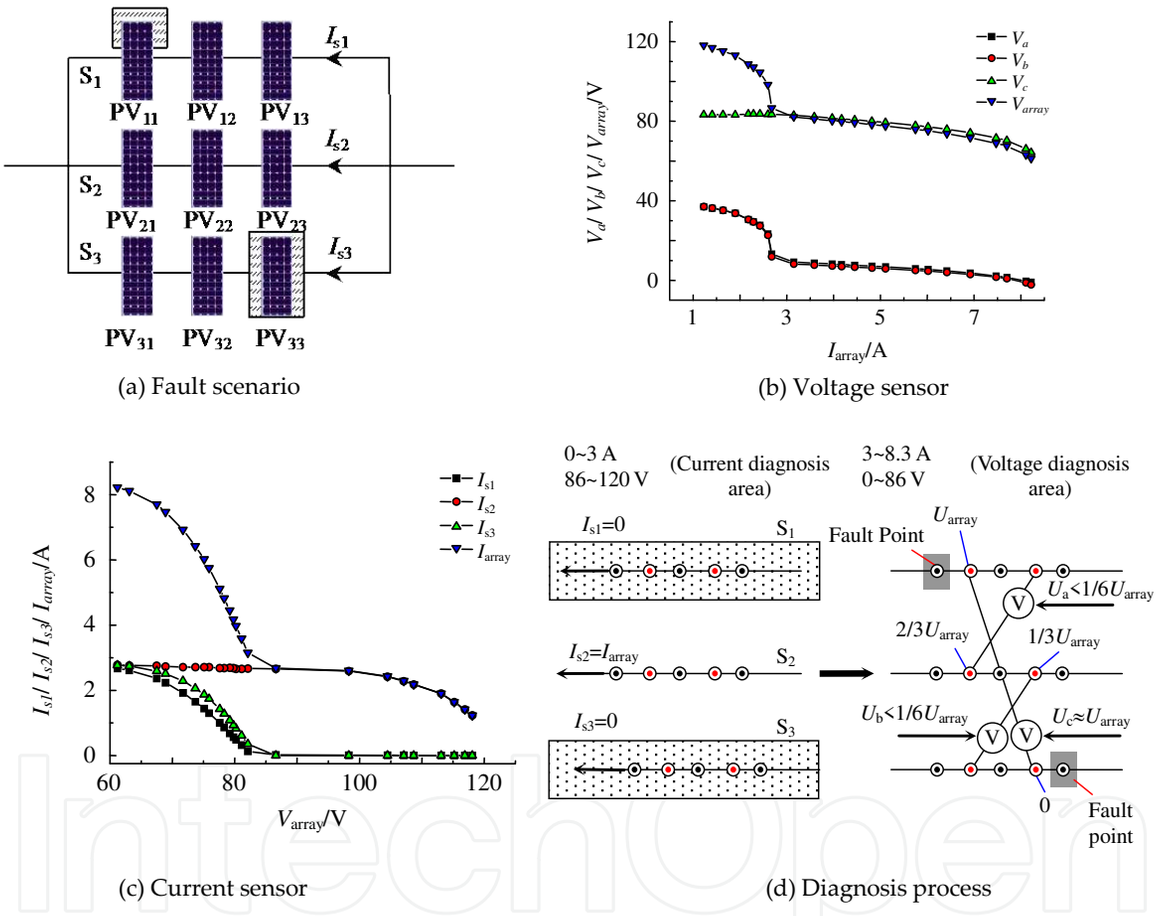

Figure 17. Multibranches mono-module fault diagnosis.

In fault scenario 3 of Fig. 18(a), the illumination is 610 W/m^2 and the temperature is 30℃. P32 and P33 in string 3 are cast by partial shadow and full shadow, respectively. Fig. 18(b) demonstrates their output characteristics. String 3 can only generate electricity over the voltage range of 0–60 V. As presented in Fig. 18(a), V_a=V_{array}/3 in the whole output voltage range, indicating that strings 1 and 2 are both healthy. In the low-voltage area, V_c matches the reference value 2V_{array}/3, verifying that P33 is faulty. In the high-voltage area, V_c=2V_{oc}-V_{array}/3. Therefore, either P31 or P32 is faulty. Fig. 18(d) presents the fault diagnosis progress.

http://dx.doi.org/10.5772/62057

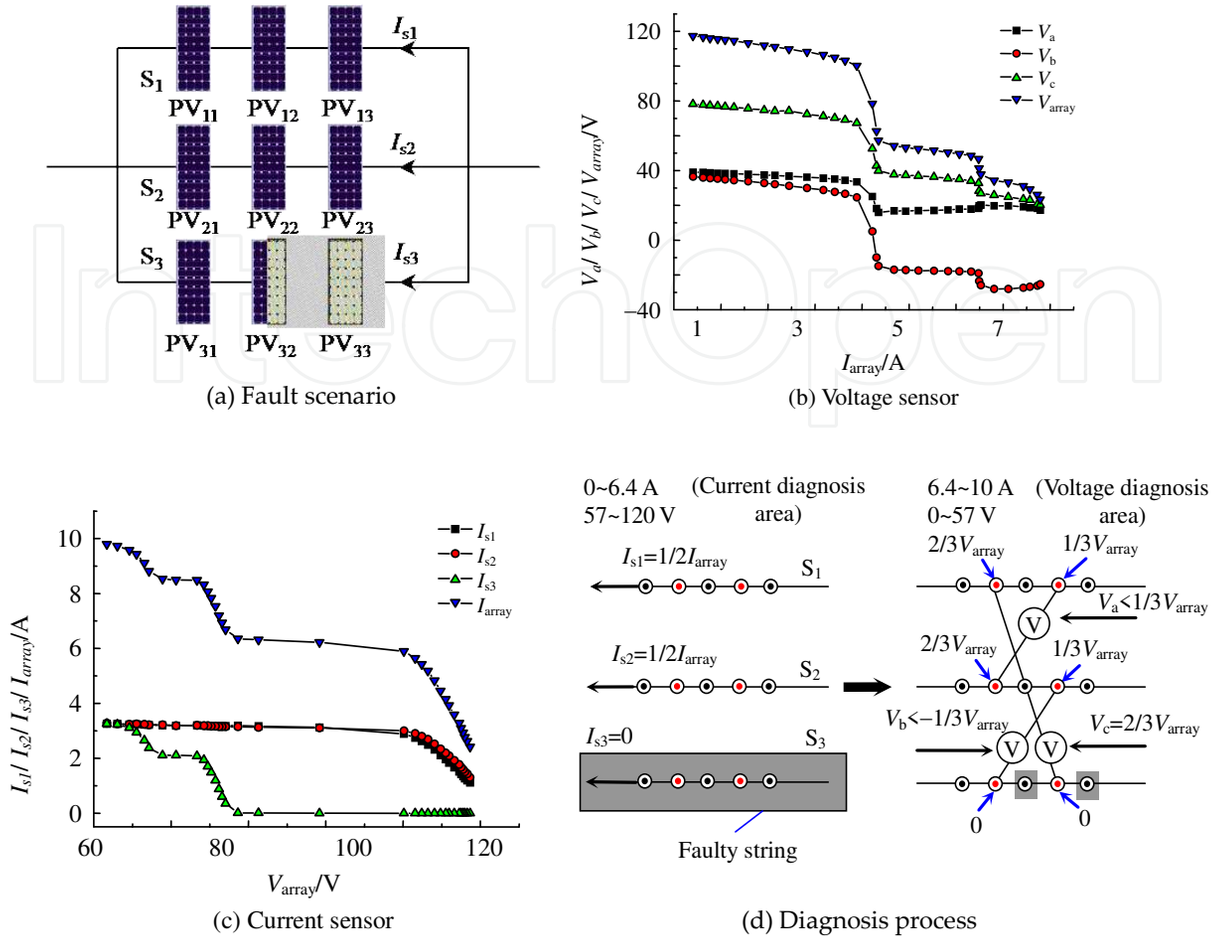

Figure 18. Mono-branch multi-module fault diagnosis.

6.2. Thermal camera-based PV fault diagnosis

Another fault diagnosis method is based on thermal images captured by thermal cameras, as shown in Fig. 19. The camera specifications are given in Table 7. Photovoltaic modules convert part of incident solar energy into electrical energy for commercial applications, with the rest being transferred to heat energy. The modeling of PV modules plays an important role in the fault diagnosis of a PV array. The objective of this section is to develop a parameter-based model of a PV module to interpret the thermal image.

In order to validate the proposed model, a scaled experimental setup was constructed as shown in Fig. 20(a). The mini-PV module used in the experiment and its respective datasheet are shown in Table 8. The type of the solar power meter used was TM-207.

Experimental tests are conducted at different load conditions, including MPP load, heavy load, light load, and partial-shading conditions. The MPP load (35 Ω) module was used to simulate the module in a healthy string working at MPP, and the 50 Ω load was used to simulate the module in fault string working at non-MPP. The sun illumination was measured at 560 W/m²

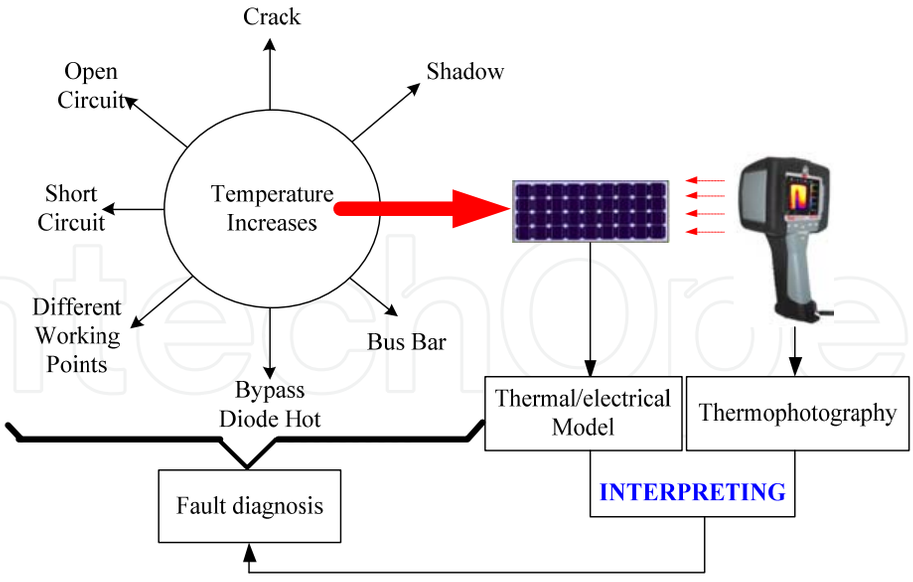

Figure 19. Schematic diagram of fault detection in PV systems.

Parameter	Value
Company	FLIR
Type	FLIR *i7*
IR resolution	140×140 pixels
Thermal sensitivity/noise equivalent temperature difference (NETD)	<0.1°C
Minimum focus distance	0.6 m
Spatial resolution (instantaneous field of view (IFOV)	3.7 mrad
Image frequency	9 Hz
Focus	Focus free

Table 7. Specifications of thermal camera

using the TM-207, and the voltage of MPP load and 50 Ω were 3.96 V and 4.37 V, respectively. The experiments were carried out at wind-speed conditions of less than 5 m/s. Fig. 20(b) is the thermography image obtained from thermal camera. Fig. 20(c) presents the Matlab processing results. The thermography produces colors by combining green, red, and blue light in varying intensities. The relationship between the constituent amounts of red, green, and blue (RGB) and the resulting color is not sensitivity. HSV method that stands for *hue*, *saturation*, and *value*, which is the common cylindrical-coordinate representation of points in an RGB color model, is introduced to process the thermography. By processing the image, the temperature difference can be clearly shown as illustrated in Fig. 20(c). Fig. 20(c) is the processing picture of Fig. 20(b).

http://dx.doi.org/10.5772/62057

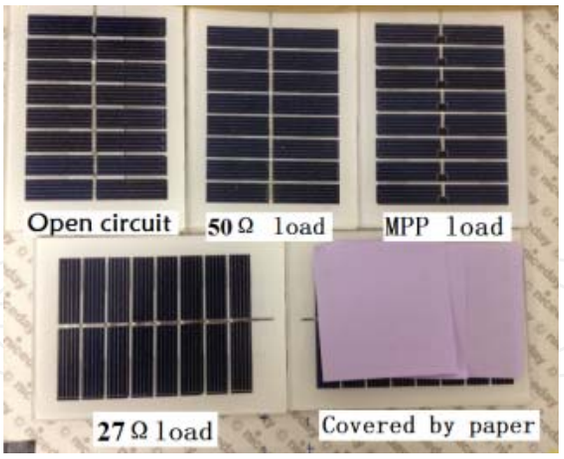

(a) Experimental setup

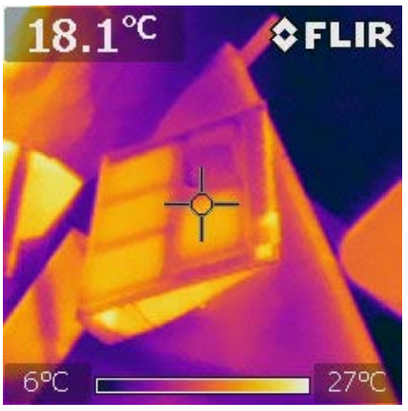

(b) Thermography

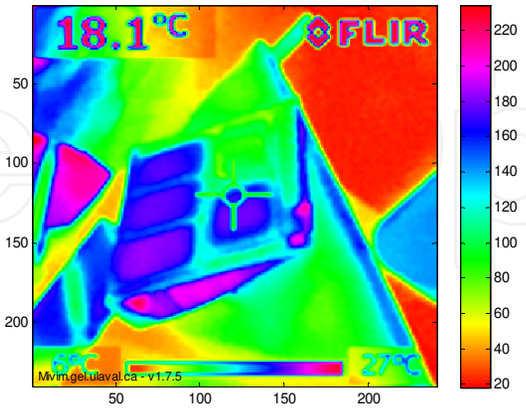

(c) Pretreatment of the thermography

Figure 20. Thermographical results at different load conditions.

Parameters	Value
Open voltage/V	4.8
Short current/A	0.23
MPP current/A	0.21
MPP voltage/V	3.85
Current temperature coefficient/℃	0.06%/K
Voltage temperature coefficient/℃	–0.36%/K
Power temperature coefficient /℃	–0.45%/K
Maximum power /W	0.8

Table 8. PV Module Parameter

7. Conclusion

This chapter has reviewed the fault mechanisms and model-based diagnosis techniques for PV systems. It can be concluded that: (i) the PV module electrical model and energy balance are coupled to establish a parameter-based model, (ii) the key parameters (S, U_{pv}, and T_a) of the PV model are calculated from two working points of the PV module and corresponding temperature, and (iii) fault diagnosis is realized by model-based methods. Notwithstanding the fact that a parameter-based model has been established and validated, other factors, such as wind and dust, which are not considered in this chapter, may contribute to the PV fault in reality. The vortex and dust distribution caused by wind can introduce non-uniform temperature distribution in the thermography. It is challenging to accurately estimate the temperature of PV modules. The pattern and features of historic information will be useful to for nonuniform illustration of PV systems.

Author details

Yihua Hu[1] and Wenping Cao[2*]

*Address all correspondence to: w.p.cao@aston.ac.uk

1 University of Strathclyde, Glasgow, UK

2 Aston University, Birmingham, UK

References

[1] Maki, A., Valkealahti, A., (2013). "Effect of photovoltaic generator components on the number of MPPs under partial shading conditions," *IEEE Transactions on Energy Conversion,* vol. 28, no. 4, pp. 1008-1017.

[2] El-Dein, M.Z.S., Kazerani, M., Salama, M.M.A., (2013). "Optimal photovoltaic array reconfiguration to reduce partial shading losses," *IEEE Transactions on Sustainable Energy*, vol. 4, no. 1, pp. 145-153.

[3] Mahmoud, Y.A., Xiao, W., Zeineldin, H.H., (2013). "A parameterization approach for enhancing PV model accuracy," *IEEE Transactions on Industrial Electronics*, vol. 60, no. 12, pp. 5708-5716.

[4] Alajmi, B.N., Ahmed, K.H., Finney, S.J., Williams, B.W., (2013). "A maximum power point tracking technique for partially shaded photovoltaic systems in microgrids," *IEEE Transactions on Industrial Electronics*, vol. 60, no. 4, pp. 1596-1606.

[5] Sullivan, C.R., Awerbuch, J.J., Latham, A.M., (2013). "Decrease in photovoltaic power output from ripple: simple general calculation and the effect of partial shading," *IEEE Transactions on Power Electronics*, vol. 28, no. 2, pp. 740-747.

[6] Patel, H., Agarwal, V., (2008). "Matlab-based modeling to study the effects of partial shading on PV array characteristics," *IEEE Transactions on Energy Conversion,* vol. 23, no. 1, pp. 302-310.

[7] Hu, Y., Cao, W., Finney, S., (2014). "Identifying PV module mismatch faults by a thermography-based temperature distribution analysis," *IEEE Transactions on Device and Materials Reliability*, vol. 14, no. 4, pp. 951-960.

[8] Hu, Y., Gao, B., Tian, G.Y., Song, X., Li, K., He, X., (2013). "Photovoltaic fault detection using a parameter based model," *Solar Energy*, vol. 96, pp. 96-102.

[9] Hu, Y., Cao, W., Ji, B., Song, X., (2015). "New multi-stage hysteresis control of DC-DC converters for grid-connected photovoltaic systems," *Renewable Energy*, vol. 74, pp. 247-254.

[10] Hu, Y., Cao, W., Wu, J., Ji, B., Holliday, D., (2014b). "Thermography-based virtual MPPT scheme for improving PV energy efficiency at partial shading conditions," *IEEE Transactions on Power Electronics,* vol. 29, no. 11, pp. 5667-5672.

[11] Tonui, J.K., Tripanagnostopoulos, Y., (2007). "Air-cooled PV/T solar collectors with low cost performance improvements," *Solar Energy*, vol. 81, no. 4, pp. 498-511.

[12] Ishaque, K., Salam, Z., Syafaruddin, A., (2011). "A comprehensive MATLAB Simulink PV system simulator with partial shading capability based on two-diode model," *Solar Energy*, vol. 85, no. 9, pp. 2217-2227.

[13] Munoz, M.A., Alonso-García, M.C., Vela, N., Chenlo, F., (2011). "Early degradation of silicon PV modules and guaranty conditions," *Solar Energy*, vol. 85, no. 9, pp. 2264-2274.

[14] Kaplani, E., (2012). "Detection of degradation effects in field-aged c-si solar cells through IR thermography and digital image processing," *International Journal of Photoenergy*, article ID: 396792, vol. 2012, pp. 11.

[15] Acciani, G., Simione, G.B., Vergura, S., (2010). "Thermographic analysis of photovoltaic panels," *International Conference on Renewable Energies and Power Quality (ICREPQ'10)*, Granada (Spain).

[16] Buerhopa, C.l., Schlegela, D., Niessb, M., Vodermayerb, C., Weißmanna, R., Brabeca, C.J., (2012). "Reliability of IR-imaging of PV-plants under operating conditions," *Solar Energy Materials and Solar Cells*, vol. 107, pp. 154-164.

[17] Parinya, P., Wiengmoon, B., Chenvidhya D., Jivacate, C., (2007). "Comparative study of solar cells characteristics by temperature measurement," *22nd European Photovoltaic Solar Energy Conference*, Milan, Italy.

[18] Krenzinger, A., Andrade, A.C., (2007). "Accurate outdoor glass thermographic thermometry applied to solar energy devices," *Solar Energy*, vol. 81, no. 8, pp. 1025-1034.

[19] Meyer, E.L., Ernest van Dyk, E., (2004). "Assessing the reliability and degradation of photovoltaic module performance parameters," *IEEE Transactions on Reliability*, vol. 53, no. 1, pp. 83-92.

[20] Simon, M., Meyer, E.L., (2010). "Detection and analysis of hot-spot formation in solar cells," *Solar Energy Materials and Solar Cells*, vol. 94, no. 2, pp. 106-113.

[21] Kurnik, J., Jankovec, M., Brecl, K., Topic, M., (2011). "Outdoor testing of PV module temperature and performance under different mounting and operational conditions," *Solar Energy Materials & Solar Cells*, vol. 95, no. 1, pp. 373-376.

[22] Zou, Z., Hu, Y., Gao, B., Woo, W.L., Zhao, X., (2014). "Study of the gradual change phenomenon in the infrared image when monitoring photovoltaic array," *Journal of Applied Physics*, vol. 115, no. 4, pp. 043522-1-11.

[23] Takashima, T., Yamaguchi, J., Otani, K., Oozeki, T., Kato, K., (2009). "Experimental studies of fault location in PV module strings," *Solar Energy Materials and Solar Cells*, vol. 93, nos. 6-7, pp. 1079-1082.

[24] Kumar, R.A., Suresh, M.S., Nagaraju, J., (2001). "Measurement of AC parameters of gallium arsenide (GaAs/Ge) solar cell by impedance spectroscopy," *IEEE Transactions on Electron Devices*, vol. 48, no. 9, pp. 2177-2179.

[25] Chouder, A., Silvestre, S., (2010). "Automatic supervision and fault detection of PV systems based on power losses analysis," *Energy Conversion and Management*, vol. 51, no. 10, pp. 1929-1937.

[26] Silvestre, S., Chouder, A., Karatepe, E., (2013). "Automatic fault detection in grid connected PV systems," *Solar Energy*, vol. 94, pp. 119-127.

[27] Gokmen, N., Karatepe, E., Silvestre, S., Celik, B., Ortega, P., (2013). "An efficient fault diagnosis method for PV systems based on operating voltage-window," *Energy Conversion and Management*, vol. 73, pp. 350-360.

[28] Lin, X., Wang, Y,. Zhu, D., Chang, N., Pedram, M., (2012). "Online fault detection and tolerance for photovoltaic energy harvesting systems," *The 2012 IEEE/ACM International Conference on Computer-Aided Design (ICCAD)*, San Jose, USA, pp. 1-6.

[29] Nguyen, D., Lehman, B., (2008). "An adaptive solar photovoltaic array using model-based reconfiguration algorithm," *IEEE Transactions on Industrial Electronics*, vol. 55, no. 7, pp. 2644-2654.

[30] Storey, J.P., Wilson, P.R., Bagnall, D., (2013). "Improved optimization strategy for irradiance equalization in dynamic photovoltaic arrays," *IEEE Transactions on Power Electronics*, vol. 28, no. 6, pp. 2946-2956.

[31] Velasco-Quesada, G., Guinjoan-Gispert, F., Pique-Lopez, R., Roman-Lumbreras, M., Conesa-Roca, A., (2009). "Electrical PV array reconfiguration strategy for energy extraction improvement in grid-connected PV systems," *IEEE Transactions on Industrial Electronics*, vol. 56, no. 11, pp. 4319-4331.

[32] Wang, Y., Lin, X., Kim, Y., Chang, N., Pedram, M., (2014). "Architecture and control algorithms for combating partial shading in photovoltaic systems," *IEEE Transactions on Computer-Aided Design of Integrated Circuits and Systems*, vol. 33, no. 6, pp. 917-929.

[33] Jonathan, S., Peter, R.W., Darren, B., (2014). "The optimized-string dynamic photovoltaic array," *IEEE Transactions on Power Electronics*, vol. 29, no. 4, pp. 1768-1776.

[34] Carotenuto, P.L., Manganiello, P., Petrone, G., Spagnuolo, G., (2014). "Online recording a PV module fingerprint," *IEEE Journal of Photovoltaics*, vol. 4, no. 2, pp. 659- 668.

[35] Lopez, O., Freijedo, F.D., Yepes, A.G., Fernandez-Comesana, P., Malvar, J., Teodorescu, R., Doval-Gandoy, J., (2010). "Eliminating ground current in a transformerless photovoltaic application," *IEEE Transactions on Energy Conversion*, vol. 25, no. 1, pp. 140-147.

IntechOpen